

Complementing CGM with Sentinel-1 InSAR data

Report for SCEC Award # 18005
Submitted May, 2019

Investigator: Yuri Fialko (SIO/UCSD)

I. Project Overview

Abstract

The SCEC Community Geodetic Model (CGM) aims to describe surface deformation in Southern California at highest possible spatio-temporal resolution and accuracy. This requires an optimal integration of GPS and InSAR data. Over the time span of SCEC5, there will be a dramatic increase in the amount of InSAR data thanks to the European Space Agency (ESA) mission Sentinel-1. Sentinel-1 mission will provide several key improvements over the existing InSAR data sets, including:

i) frequent and regular acquisitions. The nominal revisit time for the currently operational Sentinel-1A and 1B satellites is 6 days. This can be compared to the minimum revisit time of 35 days for the previous ESA missions such as ERS-1/2 and ENVISAT.

ii) A smaller revisit time not only improves temporal resolution, but also significantly reduces problems with decorrelation of the radar phase, and helps mitigate atmospheric artifacts by virtue of averaging.

iii) Wide-swath capability. 300-km-wide swathes of Sentinel-1 ensure a complete coverage of Southern California with just a few tracks.

iv) Uniform coverage from both ascending and descending satellite orbits. Data from two different look directions allow us to separate horizontal and vertical components of surface displacements.

Incorporation of Sentinel-1 data is therefore expected to result in a significant improvement of CGM. Over the last year we have set up a system for routine systematic processing of all Sentinel-1 data from Southern California. We also started generating higher-level products for integration into CGM.

SCEC Annual Science Highlights

Tectonic Geodesy

Exemplary Figure

Figure 2 or Figure 3.

SCEC Science Priorities

1a, 1e, 2a

Intellectual Merits

Interferometric Synthetic Aperture Radar (InSAR) data are increasingly used to image deformation due to active faults. One of the well-recognized limitations of InSAR measurements of the low-amplitude long-wavelength signals such as those due to interseismic deformation is increased uncertainty at wavelengths greater than several tens of kilometers. This stems from a number of factors, including imprecise knowledge of satellite orbits and regional trends in phase delays due to the signal propagation through the ionosphere and troposphere. As a result, the long-wavelength component of InSAR measurements is typically constrained to fit some auxiliary (e.g., Global Navigation Satellite System, or GNSS) data, or model assumptions. We investigated to what extent InSAR data from the current generation of InSAR satellites - in particular, the Sentinel-1 mission - are able to provide constraints on the long-wavelength tectonic deformation that are independent from those provided by the GNSS data. Toward this end, we processed a dataset used in the CGM exercise (Los Angeles/Mojave area) to generate InSAR time series. We used CANDIS method, a technique based on iterative common point stacking, to correct the InSAR data for tropospheric and ionospheric artifacts when calculating secular velocities and time series, and to isolate low-amplitude deformation signals in the study region. We compared data collected by Sentinel-1 between 2014-2019 with continuous GPS measurements, and computed the average line of sight (LOS) displacements over the respective epoch. The two data sets showed a reasonable agreement, indicating that the InSAR data can reliably measure deformation signals at wavelengths on the order of 10^2 km. Data from overlapping InSAR tracks with different look geometries can be combined with information on the local azimuth of the horizontal velocity vector (e.g., from the continuous GPS measurements) to obtain the 3 orthogonal components of surface motion.

Broader Impacts

Evaluation of seismic hazard is based primarily on historic seismicity and long-term fault slip rates inferred from paleoseismic data. Geodetic observations provide an important additional source of information about contemporaneous accumulation of strain in the seismogenic layer. UCERF3 model now incorporates estimates of fault slip rates based on geodetic data. A major outstanding question is whether geodetic observations can help identify areas of seismic hazard that haven't been recognized based on available seismic and geologic data. While mature faults such as the San Andreas fault by and large have clear expression in geomorphology, young developing faults and fault zones may be more difficult to recognize. Sentinel-1 InSAR data will help us better understand a potential contribution of geodetic observations to estimates of seismic hazard such as UCERF. The proposed collection and analysis of space geodetic data will improve our understanding of the associated seismic hazard to populated areas in Southern California. This project has provided training and support for one graduate student.

II. Technical Report

InSAR measurements of low-amplitude (sub-centimeter) deformation are chiefly limited by contributions to the radar phase due to ionosphere, troposphere, and imprecise knowledge of satellite orbits (*Goldstein 1995; Jehle et al. 2010; Meyer 2011; Tarayre and Massonnet 1996; Zebker et al. 1997*). The ionospheric phase delays are caused by the varying density of charged particles at altitudes of about 50-1000km, while the tropospheric phase delays are dominated by variations in pressure and water content in the lowermost 10-20km of the atmosphere (*Bevis et al. 1992*). The methods proposed for the reduction of the propagation artifacts include averaging of multiple independent interferograms to suppress uncorrelated noise in the radar phase (*Fialko 2006; Peltzer*

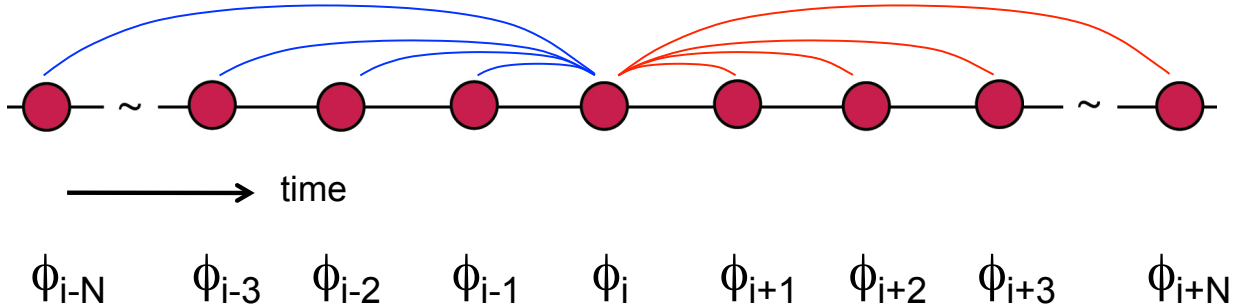


Figure 1: A diagram illustrating the common-point stacking algorithm to evaluate the propagation (atmospheric, ionospheric) and orbital contributions to the radar phase ϕ on an acquisition date i .

et al. 2001; *Wright et al.* 2004), spatio-temporal filtering (*Berardino et al.* 2002; *Ferretti et al.* 2001; *Schmidt and Bürgmann* 2003), wavelet decomposition (*Hetland et al.* 2012), as well as the use of auxiliary meteorologic and other data. Unfortunately, accurate estimates of water vapor in the atmosphere are not yet available at a sufficient spatiotemporal resolution worldwide. The same holds for estimates of the Total Electron Content (TEC) in the ionosphere that could be used to estimate ionospheric phase delays. We use a recently developed method for the calculation of noise due to atmospheric, ionospheric, and orbital artifacts directly from the SAR data (*Tymofyeyeva and Fialko* 2015). Our algorithm exploits the fact that interferograms that share a common scene necessarily contain the same contributions from delays in the radar phase due to propagation effects. The scheme entails the following steps:

1. Generate a set of interferograms for a given range of perpendicular baselines and time spans.
2. Select a subset of interferograms with sufficient correlation and coverage.
3. Evaluate Atmospheric Noise Coefficients (ANC) for each SAR acquisition. We do so by subdividing the interferometric “connectivity tree” into triplets, and computing the L_2 norm of range changes for every interferogram, as well as for sums of sequential interferograms sharing a common scene. The root mean square (RMS) of the de-trended range changes ($\Delta\rho$), defined as

$$RMS = \sqrt{\frac{1}{N} \sum_{i=0}^N (\Delta\rho_i - T_i)^2}, \quad (1)$$

where N is the number of valid pixels and T is some best-fitting trend (e.g., a quadratic surface, or some other predictor of zero mean), characterizes the power of the signal in each interferogram. Equation (2) illustrate how the Atmospheric Noise Coefficient (ANC) is defined for each acquisition:

$$ANC_i = (10.0) (R_{max})^{-1} \sqrt{\frac{1}{M} \sum_{m=1}^M (\alpha_i(x_m) - \bar{\alpha}_i)^2} \quad (2)$$

where $\alpha_i(x_m)$ is the atmospheric phase delay at the pixel m on the date i , and $\bar{\alpha}_i = M^{-1} \sum_{m=1}^M \alpha_i(x_m)$ is the mean value of the atmospheric phase taken over all M pixels. R_{max} represents the RMS (root mean square) value of the phase screen with the highest amount of noise, and is used to normalize the ANC values on a scale between 0 and 10. The ANC quantifies the relative amount of atmospheric noise at each SAR acquisition, and allows us to rank the acquisitions according to the magnitude of atmospheric contribution. In the next iteration, we recalculate α for each

scene, starting with the noisiest date and using previously calculated atmospheric phase estimates to correct the interferograms used in the calculation of α for subsequent dates. The accuracy of the atmospheric phase estimates decreases toward the ends of the catalog, where shorter and/or one-sided averaging stencils need to be used. Such scenes are typically excluded from the subsequent time series analysis.

4. Compute atmospheric phase screens for all shared scenes by stacking interferograms that share the respective scene, making sure that the sign of interferograms that span later time periods is opposite to those of the earlier period, so that the atmospheric contribution is enhanced. Figure 1 illustrates the respective algorithm. We begin stacking for the atmospheric phase screens for the acquisitions with the largest ANCs. The computed phase screens are then subtracted from the interferograms used to estimate phase screens for the remaining acquisitions. The ANCs are then updated by computing RMS of the de-tended (zero-mean) atmospheric phase screens. The accuracy of the atmospheric phase estimates decreases toward the ends of the catalog, where shorter and/or one-sided averaging stencils need to be used. The procedure is repeated iteratively until the results converge with the prescribed tolerance.

Because ionospheric contributions and long-wavelength “ramps” due to incorrect orbital information have the same property of changing sign in the shared interferograms, they can be estimated using the same procedure. An essential point for the orbital error estimates is that the interferograms are not “flattened” during processing, and are generated using the original state vectors. This approach would be exact given a sufficiently large number of SAR acquisitions with regular intervals and good radar coherence between nearest data takes. Both conditions appear to be met in case of Sentinel-1 data.

We have validated our method by inverting synthetic data that contain realistic atmospheric noise and a known deformation signal, as well as by comparisons of InSAR and GPS time series (*Tymofeyeva and Fialko 2015*). Among the limitations of the previous (ERS-1/2, ENVISAT, ALOS-1) data sets are uneven coverage from the ascending and descending orbits, relatively narrow swathes (resulting in discontinuities in the LOS velocities across the swath boundaries), and large uncertainties in the satellite orbits. Sentinel-1 data are more optimal for measuring interseismic deformation due to larger (by a factor of 3) swath width, regular data takes, and accurate orbits.

To investigate the accuracy of Sentinel-1 measurements at large (>50 km) wavelengths, we used a data set from the CGM exercise (ascending track 64 and descending track 71 that span the Los Angeles area and the Southern Mojave desert). We have generated sequential interferograms that cover the area of study over a time period of 4 years between 2014 and early 2019. The data were processed using GMTSAR (*Xu et al. 2016*). All radar images were aligned to a single master using the bivariate enhanced spectral diversity (BESD) method (*Wang et al. 2017*). Tightly controlled baselines of Sentinel-1 satellites ensure that all acquisitions can be interfered with their immediate neighbors. After applying the atmospheric corrections, we generated timeseries of LOS displacements for every coherent pixel in each track. To compare the InSAR time series to the GPS data, we referenced both data sets to the continuous GPS site AGMT. Figure 2 shows a comparison of the InSAR and GPS timeseries of the LOS displacement between two continuous GPS sites, AGMT and P587. To enable this comparison, the three components of the displacement vector measured with GPS were projected onto the respective line of sight (taking into account the local incidence angle). As one can see from Figure 2, the InSAR timeseries reveal some quasi-periodic features, most likely due to variations in the water content in the troposphere that are correlated in time (e.g., due to seasonal cycles). Nevertheless, linear fits to the InSAR timeseries (black dashed lines) for this, as well as for other pairs of the GPS sites closely follow the trends in the GPS timeseries, suggesting that the interseismic velocities recorded by the two independent data sets are in a reasonably good agreement.

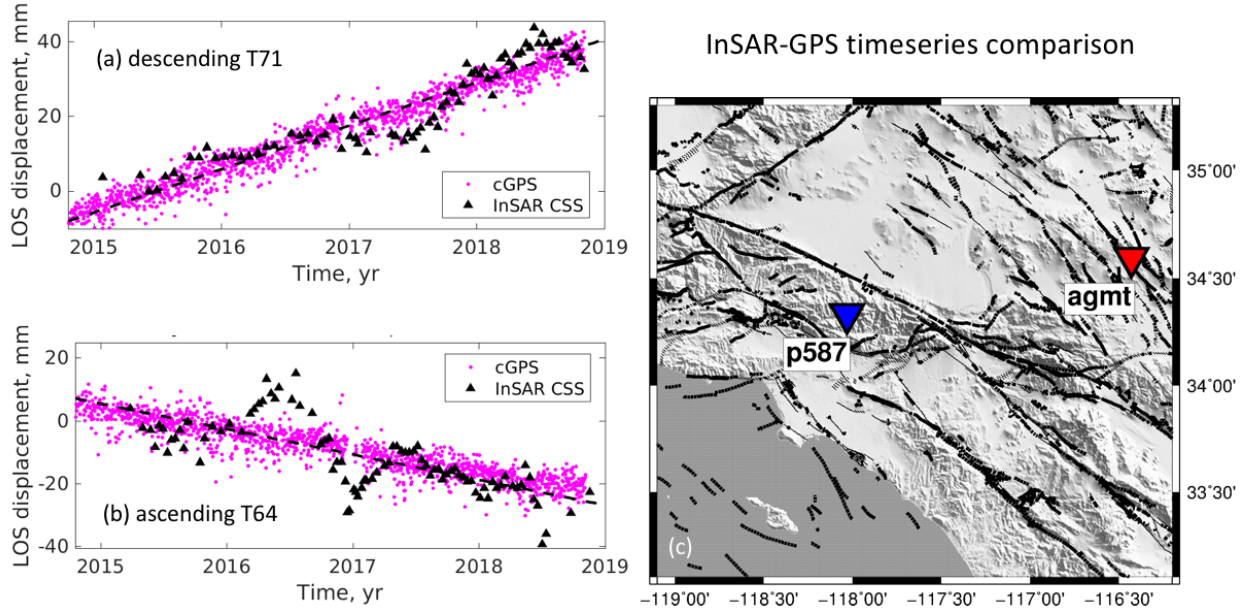


Figure 2: (a, b) Timeseries of LOS displacements between the continuous GPS sites AGMT and P587 (see panel c). Black triangles denote the InSAR Sentinel-1 data and magenta dots denote the GPS data. Black dashed lines denote the least square linear fit to the InSAR timeseries.

We then computed the average LOS velocities by fitting straight lines to the InSAR timeseries at every pixel. The resulting map of the average LOS velocities for the descending track 71 is shown in Figure 3. Results shown in Figure 3 reveal a pattern expected of interseismic deformation in Southern California, with increases in the radar range across the main plate boundary faults such as the San Andreas fault.

LOS displacements or velocities such as those shown in Figure 3 can be used to compute the vertical and horizontal components following the procedure described in *Lindsey et al. (2014)* and *Tymofyeyeva and Fialko (2018)*. This procedure relies on an additional constraint on the azimuth of the horizontal displacement vector. This constraint can be obtained from the interpolated horizontal (East and North) components of the velocity field provided by the continuous GPS data (*Tymofyeyeva and Fialko 2018*).

The resulting 3-component velocity maps will provide a useful input into CGM. In particular, a robust and accurate characterization of vertical deformation of the Earth's surface is an important component of CGM, yet so far it has proven difficult as continuous GPS data are less sensitive to the vertical component of deformation compared to the horizontal component. The InSAR data are, on the other hand, highly sensitive to vertical motion. Thus an optimal combination of InSAR and GPS data will be able to produce a high-resolution map of vertical velocity over Southern California. The signal-to-noise ratio will further improve as more data are incorporated in the analysis.

This project provided training and support for one graduate student (Zeyu Jin) who is finishing his second year at SIO.

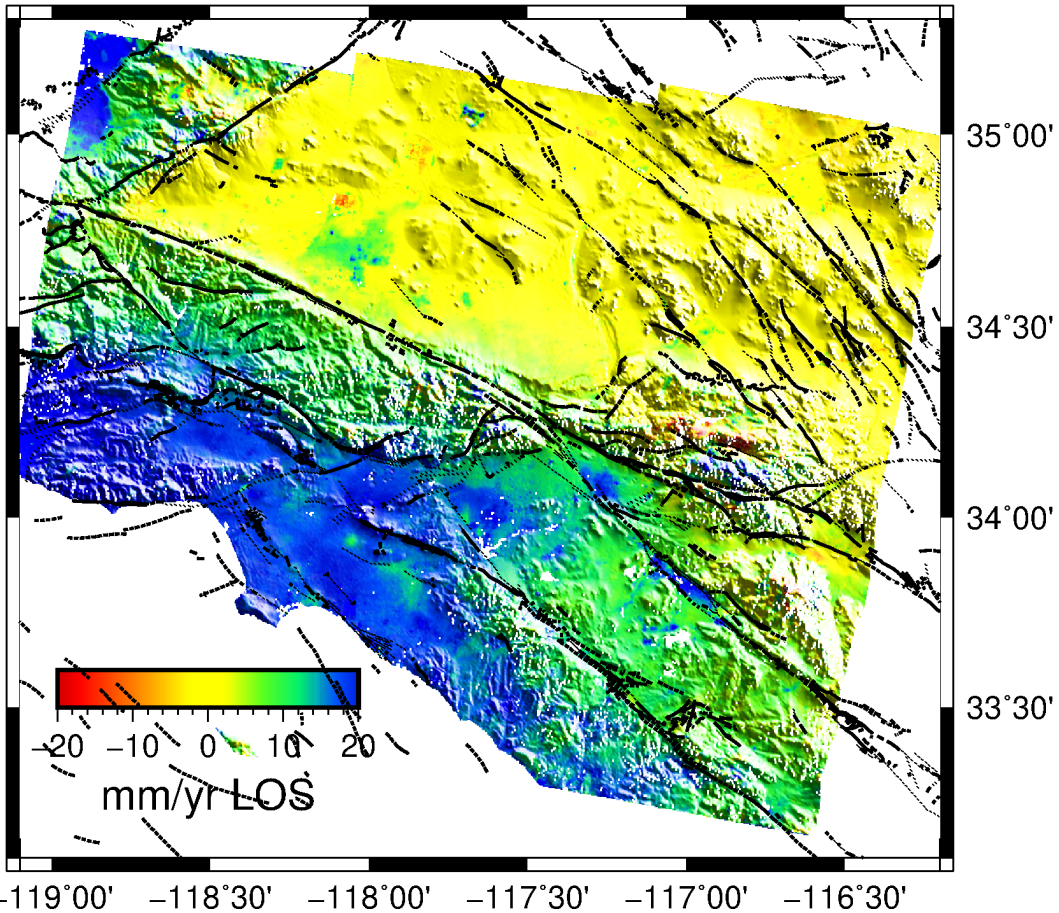


Figure 3: Secular LOS velocity for the descending Sentinel-1 track 71. Motion toward the satellite (range decrease) is considered positive.

References

- Berardino, P., G. Fornaro, R. Lanari, and E. Sansosti, A new algorithm for surface deformation monitoring based on small baseline differential SAR interferograms, *IEEE Transactions on Geoscience and Remote Sensing*, 40(11), 2375–2383, doi:10.1109/TGRS.2002.803792, 2002.
- Bevis, M., S. Businger, T. A. Herring, C. Rocken, R. A. Anthes, and R. H. Ware, GPS meteorology: Remote sensing of atmospheric water vapor using the global positioning system, *Journal of Geophysical Research*, 97(D14), 15,787, doi:10.1029/92JD01517, 1992.
- Ferretti, A., C. Prati, and F. Rocca, Permanent scatterers in SAR interferometry, *IEEE Transactions on Geoscience and Remote Sensing*, 39(1), 8–20, doi:10.1109/36.898661, 2001.
- Fialko, Y., Interseismic strain accumulation and the earthquake potential on the southern San Andreas fault system., *Nature*, 441(7096), 968–971, doi:10.1038/nature04797, 2006.
- Goldstein, R., Atmospheric limitations to repeat-track radar interferometry, *Geophysical Research Letters*, 22(18), 2517–2520, doi:10.1029/95GL02475, 1995.
- Hetland, E. A., P. Musé, M. Simons, Y. N. Lin, P. S. Agram, and C. J. DiCaprio, Multiscale InSAR Time Series (MInTS) analysis of surface deformation, *Journal of Geophysical Research: ...*, 117(B2), B02,404, 2012.
- Jehle, M., O. Frey, D. Small, and E. Meier, Measurement of Ionospheric TEC in Spaceborne SAR Data, *IEEE Transactions on Geoscience and Remote Sensing*, 48(6), 2460–2468, doi:10.1109/TGRS.2010.2040621, 2010.
- Lindsey, E. O., Y. Fialko, Y. Bock, D. T. Sandwell, and R. Bilham, Localized and distributed creep along the southern San Andreas Fault, *Journal of Geophysical Research: Solid Earth*, 119(10), 7909–7922, doi:10.1002/2014JB011275, 2014.
- Meyer, F. J., Performance Requirements for Ionospheric Correction of Low-Frequency SAR Data, *IEEE Transactions on Geoscience and Remote Sensing*, 49(10), 3694–3702, doi:10.1109/TGRS.2011.2146786, 2011.
- Peltzer, G., F. Crampé, S. Hensley, and P. Rosen, Transient strain accumulation and fault interaction in the Eastern California shear zone, *Geology*, 29(11), 975, doi:10.1130/0091-7613(2001)029<0975:TSAAFI>2.0.CO;2, 2001.
- Schmidt, D. A., and R. Bürgmann, Time-dependent land uplift and subsidence in the Santa Clara valley, California, from a large interferometric synthetic aperture radar data set, *Journal of Geophysical Research*, 108(B9), 2416, doi:10.1029/2002JB002267, 2003.
- Tarayre, H., and D. Massonnet, Atmospheric Propagation heterogeneities revealed by ERS-1 interferometry, *Geophysical Research Letters*, 23(9), 989–992, doi:10.1029/96GL00622, 1996.
- Tymofyeyeva, E., and Y. Fialko, Mitigation of atmospheric phase delays in InSAR data, with application to the eastern California shear zone, *Journal of Geophysical Research: Solid Earth*, 120(8), 5952–5963, doi:10.1002/2015JB011886, 2015JB011886, 2015.
- Tymofyeyeva, E., and Y. Fialko, Geodetic Evidence for a Blind Fault Segment at the Southern End of the San Jacinto Fault Zone, *Journal of Geophysical Research: Solid Earth*, 123(1), 878–891, doi:10.1002/2017JB014477, 2018.
- Wang, K., X. Xu, and Y. Fialko, Improving burst alignment in TOPS interferometry with bivariate enhanced spectral diversity (BESD), *IEEE Geoscience and Remote Sensing Letters*, 14, 2423–2427, 2017.
- Wright, T. J., B. Parsons, P. C. England, and E. J. Fielding, InSAR observations of low slip rates on the major faults of western Tibet., *Science (New York, N. Y.)*, 305(5681), 236–9, doi:10.1126/science.1096388, 2004.
- Xu, X., D. Sandwell, E. Tymofyeyeva, A. González-Ortega, and X. Tong, Tectonic and Anthropogenic Deformation at the Cerro Prieto Geothermal Step-Over Revealed by Sentinel-1A InSAR, *IEEE Transactions on Geoscience and Remote Sensing*, 55, 5284–5292, 2016.
- Zebker, H. A., P. A. Rosen, and S. Hensley, Atmospheric effects in interferometric synthetic aperture radar surface deformation and topographic maps, *Journal of Geophysical Research*, 102(B4), 7547, doi:10.1029/96JB03804, 1997.